

Enhanced ionic diffusion in ionomer-filled nanopores

Elshad Allahyarov, Philip L. Taylor, and Hartmut Löwen

Citation: *The Journal of Chemical Physics* **143**, 243126 (2015); doi: 10.1063/1.4935114

View online: <http://dx.doi.org/10.1063/1.4935114>

View Table of Contents: <http://scitation.aip.org/content/aip/journal/jcp/143/24?ver=pdfcov>

Published by the [AIP Publishing](#)

Articles you may be interested in

[Biphilic nanoporous surfaces enabled exceptional drag reduction and capillary evaporation enhancement](#)
Appl. Phys. Lett. **105**, 191611 (2014); 10.1063/1.4901962

[Wetting transitions of polymers via thermal and plasma enhanced atomic layer depositions](#)
J. Vac. Sci. Technol. A **31**, 01A147 (2013); 10.1116/1.4772666

[Structure and dynamics of liquid methanol confined within functionalized silica nanopores](#)
J. Chem. Phys. **133**, 154707 (2010); 10.1063/1.3503886

[Water filling of hydrophilic nanopores](#)
J. Chem. Phys. **133**, 034513 (2010); 10.1063/1.3462964

[Water diffusion and fracture behavior in nanoporous low- \$\kappa\$ dielectric film stacks](#)
J. Appl. Phys. **106**, 033503 (2009); 10.1063/1.3187931



AIP | APL Photonics

APL Photonics is pleased to announce
Benjamin Eggleton as its Editor-in-Chief



Enhanced ionic diffusion in ionomer-filled nanopores

Elshad Allahyarov,^{1,2,3,4,a)} Philip L. Taylor,⁵ and Hartmut Löwen¹

¹*Institut für Theoretische Physik II: Weiche Materie, Heinrich-Heine Universität Düsseldorf, Universitätsstrasse 1, 40225 Düsseldorf, Germany*

²*Department of Macromolecular Science and Engineering, Case Western Reserve University, Cleveland, Ohio 44106-7202, USA*

³*Theoretical Department, Joint Institute for High Temperatures, Russian Academy of Sciences (IVTAN), 13/19 Izhorskaya Street, Moscow 125412, Russia*

⁴*International Research Centre, Baku State University, Baku, Azerbaijan*

⁵*Department of Physics, Case Western Reserve University, Cleveland, Ohio 44106-7079, USA*

(Received 6 August 2015; accepted 20 October 2015; published online 13 November 2015)

Coarse-grained simulations in the united-atom-model approximation are used to investigate confinement-induced morphological changes in Nafion-like ionomers. The system we study models a cylindrical pore in a hydrophobic matrix of supporting material with pore diameters that vary from 0.7 to 3.96 nm. Simulation results indicate a strong dependence of the equilibrium ionomer structures both on the pore diameter and on the sulfonate concentration in the pore. In the case of larger pores, the ionic clustering has the shape of a branched wire-like network oriented parallel to the pore axis. In the case of narrow pores, the ionic clusters occupy the pore center and exhibit strong density modulations both along the pore axis and across the pore diameter. The calculated diffusion coefficients for the ions indicate a sharp increase within the narrow pores. This finding is explained by ballistic-type ionic motion at shorter times and by the collective motion of ions in hydrophilic clusters. The influence of the hydrophobic walls on the distribution of ions and solvent molecules is discussed. © 2015 AIP Publishing LLC. [<http://dx.doi.org/10.1063/1.4935114>]

I. INTRODUCTION

Ionomers are used as polymer electrolyte membrane (PEM) separators in fuel cell applications and hydrogen energy technologies.^{1–6} The high ionic conductivity of contemporary ionomers, typically Nafion® (a Dupont co-polymer of tetrafluoroethylene (Teflon®) and perfluoro-3,6-dioxo-4-methyl-7-octene-sulfonic acid) and its substitutes, is achieved when the PEM membrane is highly hydrated. In a hydrated PEM, the terminal-group hydrogens dissociate from their host sulfonates. The latter self-assemble into connected clusters creating hydrophilic pathways inside the hydrophobic Teflon backbone matrix. Within the pathways, en-masse and Grotthuss-related diffusion of conducting ions takes place.^{7–9} The existence of high water content in hydrated ionomers, however, makes the membrane vulnerable to solvent freezing and boiling at low and high temperatures, respectively.^{10,11} Under excessive hydration conditions, the swollen membranes lose their elastic properties and become increasingly permeable to the fuel (hydrogen or methanol) and to contaminants.¹² The increased diffusion of ions at high hydration levels also makes the ionomer membranes prone to rapid dehydration, which causes irreversible structural changes in the membrane.

Possible solutions to the problem of membrane degradation at high water contents are based on the development of new composite membranes that can either retain their hydration level at high temperatures or maintain their transport properties and performance under conditions of low humidity.^{13,14}

Usually for this purpose, the pure ionomer is mixed with functional additives which, in addition to facilitating the formation of effective ionic pathways, can also provide sufficient ionic and solvent mobilities under harsh operating conditions. The additives might be either functional nanoparticles embedded in the bulk ionomer or a porous matrix hosting the ionomer. The latter, called a *matrix reinforced ionomer*, or mechanically reinforced membrane, is considered a promising technology for a new generation of fuel cells. For example, in recent years new products such as the Gore-Select membrane (W. M. Gore, Inc.) and the DuPont NAFION XL 100 membrane have appeared in the market. Both of these products employ the basic idea of filling the pores of the PTFE (Teflon) matrix with hydrated ionomers. This simple approach guarantees the ionomer stability at high T and provides sufficient ion diffusion under low-water-content conditions.

The role of cylindrical confinement in determining the polymer morphology was experimentally studied for block-copolymers in Ref. 15 and for Nafion in Ref. 16. In both cases, the pores were large, being about 100–200 nm in diameter. In Ref. 17, it was shown that the reduced proton conductivity of Nafion in pores with diameters larger than 80 nm was mostly due to the diminished connectivity between sulfonate clusters and the restricted movement of the sidechains. In much smaller pores of about 3 nm diameter inside ceramic membranes of SiO₂ or TiO₂, the proton conductivity shows a steep decrease when the relative humidity in the pore decreases.¹⁸ While there is not yet a firm understanding of how the ionomer morphology depends on the pore size, and what type of morphology provides better conductivity in porous membranes, some indirect answers to this question can be found in the literature.

^{a)} Author to whom correspondence should be addressed. Electronic mail: elshad.allakhyarov@case.edu

First, as shown in Ref. 19, a hydrated Nafion membrane under operational conditions develops long, parallel, but otherwise randomly packed water channels of diameter about 2–3 nm. These channels are surrounded by partially hydrophilic sidechains. Such *inverted-micelle* water cylinders provide smooth ionic transport through the membrane.

Second, as shown in Ref. 20, in single walled carbon nanotubes, which are hydrophobic pores several nanometers in diameter, the flow rate of the solvent is higher than in larger tubes. This was explained by the formation of oriented bonds between water molecules as a “single-file” limit is approached in narrow pores. Each water in this case has only two bonds—one with the water before it and one with the water behind it—which greatly increases its mobility.

Third, the possibility of having good ionic conductivity in one-dimensional ionomers can be deduced from our previous simulations^{21–28} and from other theoretical works.^{29–32} For example, as we have shown in Refs. 22 and 25, poling of the ionomer results in the formation of hexatically ordered cylindrical channels of sulfonates, which provides higher proton diffusion than in untreated membranes. Such ordered structures, when artificially sustained by the restricting walls of the porous matrix, can withstand elevated temperatures.

In the following, we consider three Nafion-like ionomers with different backbone segment lengths L_b . According to our previous findings,^{26,28} the parameter L_b controls the shape of the sulfonate clustering network in the membrane. It defines the size of sulfonate clusters, the distance between the clusters, and the average separation between the sulfonates inside each cluster. Lower values of L_b correspond to higher sulfonate concentrations, which indirectly implies a smaller separation between the sulfonates in a cluster. Although high-sulfonate ionomers in bulk are mechanically unstable, this is not an issue in matrix-reinforced membranes.

In this work, we analyze the morphological changes found in ionomers that are restricted within cylindrical pores. Our aim is to understand how the ionic diffusion depends on the pore size and on the sulfonate density in the pore. We will show that there are optimal conditions for achieving significantly enhanced ionic diffusion in narrow pores. The rest of this paper is organized as follows. In Section II, we describe our coarse-grained model and the force-field parameters used in the ionomer simulations. The details of our Molecular dynamics (MD) simulations and the simulation run parameters are given in Section III. The simulation results for the spatial distribution of the ionic clusters, the modulation of the ionic densities, and the emergence of enhanced diffusion in narrow pores are discussed in Section IV. Our conclusions are given in Section V.

II. COARSE-GRAINED MODEL AND FORCE-FIELD PARAMETERS

The chemical structure of Nafion, an ionomer molecule consisting a Teflon backbone with attached sidechains, is shown in Fig. 1. In its dry form the terminal groups end with attached ions (hydrogen atoms). When the Nafion is hydrated beyond the $\lambda \geq 3$ levels, where λ is the number of water molecules H_2O per sulfonate group SO_3 , the ions dissociate

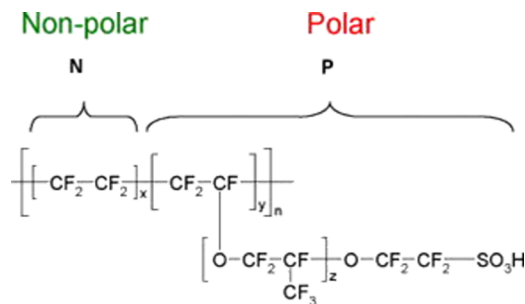


FIG. 1. Chemical structure of Nafion. The ionomer A with the backbone segment length $L_b = 14$ from Table I corresponds to $y = 1$ and $x = 6.5$. The ionomer B with the backbone segment length $L_b = 8$ from Table I corresponding to $y = 1$ and $x = 3.5$. The ionomer C with the backbone segment length $L_b = 4$ from Table I corresponding to $y = 1$ and $x = 1.5$.

from their host groups. In our molecular dynamics simulations, we coarse-grain the hydrated ionomer using a united-atom representation for the CF_2 and CF_3 groups, for the sulfur atom S, and for the oxygen group O_3 of the terminal groups.^{33–35} The coarse-graining we employ differs from the more drastic mesoscale approximations in which the entire sidechain is replaced by a single large hydrophilic blob.^{36–39} The latter approach, frequently used for probing membrane morphology, does not properly describe the ionic diffusion through the membrane.⁴⁰ Our united-atom approach also differs from the all-atomistic ionomer simulations that are usually employed to investigate the diffusion and hydration of the ions and sidechain terminal groups, but which are restricted to small ionomer systems consisting of only a few separate Nafion oligomers.^{33,41,42} By use of our united-atom approximation, sufficiently large ionomer systems, up to sizes of 10–20 nm, can be simulated. Such large system sizes are necessary for the proper description of ionic diffusion in a membrane. The details of our approach are given elsewhere,^{24–26,28} and so here we restrict ourselves to an abbreviated description of the model employed.

In our model, schematically illustrated in Fig. 2, there are $L_s = 8$ united-atom monomers per sidechain in the solvated

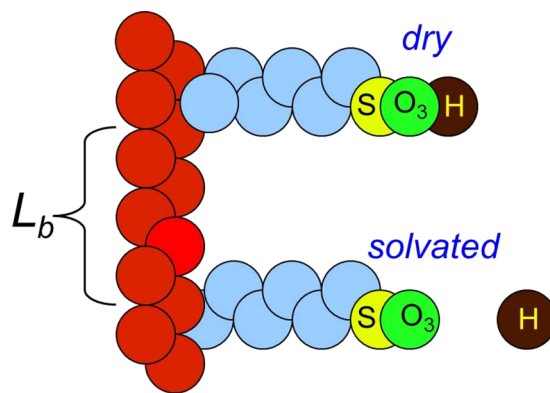


FIG. 2. Schematic representation of the united atom model for the Nafion-like ionomer. The Teflon backbone monomers, which are neutral and hydrophobic, are shown as red circles. The parameter L_b denotes the backbone segment length between adjacent sidechains. The sidechain monomers, which are also hydrophobic and neutral, are shown in blue. The sidechain terminal group SO_3 is shown as yellow and green monomers; they are charged and hydrophilic. In the hydrated state of the ionomer, the hydrogen ion is detached from its host sulfonate.

ionomer. The first six monomers are hydrophobic and the last two units, which represent a sulfur atom S and the oxygen group O₃, are hydrophilic.⁴³ For the sidechain monomers, we consider a simple charge distribution model:²⁷ a charge of $+1.1|e|$ is placed on each S unit (with e the charge of an electron) and a charge of $-2.1|e|$ on each O₃ unit. The total charge of a single sulfonate head group SO₃⁻ is $-|e|$. The remaining sidechain monomers have zero charge. This simple approach makes our simulations much faster than those assuming a partial charge distribution along the sidechain monomers.⁴⁴ This simplification appears permissible since, according to our findings in Ref. 27, the development of hydrophilic pathways in the membranes mostly depends on the amplitude of the poling field rather than on the sidechain charge distribution. All the united-atom units are modeled as Lennard-Jones (LJ) monomers with a diameter $\sigma = 0.35$ nm. We consider a fixed hydration level, $\lambda = 3$, which is large enough to permit the detachment of a hydrogen atom from its host sulfonate.³² We further assume that a detached hydrogen captures a water molecule to become a hydronium ion. The latter is modeled as a unit with a charge $|e|$ and size $\sigma = 0.35$ nm.

The total interaction potential in the membrane is a combination of electrostatic Coulomb interactions between charged pairs and the 6-12 LJ interactions between all monomers. The ionomer constituents are additionally subjected to stretching, bending, and dihedral forces. The force field details are given in our previous work^{23,24,26} and agree in most instances with the Nafion model of Paddison.⁴³ A brief description of the force field includes four components.

First, the total potential energy of the membrane is

$$U(\vec{r}) = \sum_i U_b^i + \sum_j U_\theta^j + \sum_m U_\varphi^m + \sum_{k,l} U_{nb}(|\vec{r}_k - \vec{r}_l|), \quad (1)$$

where $(\vec{r}_1, \vec{r}_2, \dots, \vec{r}_N)$ are the three-dimensional position vectors of the N particles in the system, i in the two-body bond-stretching potential U_b^i runs over all bonds, j in the three-body angle-bending potential U_θ^j runs over all bond angles, m in the four-body dihedral component of the interaction energy runs over all torsional angles, and k, l in the non-bonded (Lennard-Jones and Coulomb) potential run over all force-center pairs in the system. Second, the water is modeled as a TIP3P liquid,^{26,45} which has explicit charges $q_H = +0.417|e|$ on the hydrogen atom, and $q_O = -2q_H$ on the oxygen atom. The distance between hydrogen and oxygen atoms is $r_{OH} = 0.0957$ nm, and the angle between OH bonds is $\theta_{HOH} = 104.52^\circ$. The TIP3P model does not allow for inclusion of the non-classical Grotthuss transport of protons, but this omission will not significantly affect our simulation results at low water content λ . It is recognized that at low λ the hydronium ions are close to the sulfonates and basically move in the electrostatic energy landscape of the latter.^{8,36} The ion transport in this case also involves the sidechain rearrangement,⁴⁶ which is a built-in feature of our simulations.

Third, standard Lorentz-Berthelot combining rules are used in the LJ interactions between monomers i and j such that the interaction potential between units i and j has a minimum at the separation distance $r_{ij} = 2^{1/6}\sigma_{ij}$ where σ_{ij} is defined as $\sigma_{ij} = (\sigma_{ii} + \sigma_{jj})/2$, and the depth of the interaction at this minimum is $\epsilon_{ij} = \sqrt{\epsilon_{ii}\epsilon_{jj}}$.

Fourth, the wall-monomer interaction is treated using the particle-micropore interaction potential given by Tjatjopoulos *et al.* in Ref. 47 and further developed in Ref. 48. The interaction potential is defined as

$$U_w(x, R^*) = \pi^2 \epsilon_{wall} \left[\frac{63}{32} \frac{F_1}{(2x - x^2/R^*)^{10}} - \frac{3F_2}{(2x - x^2/R^*)^4} \right], \quad (2)$$

where $F_1 = F \left[\frac{-9}{2}, \frac{-9}{2}, 1; (1 - x/R^*)^2 \right]$, $F_2 = F \left[\frac{-3}{2}, \frac{-3}{2}, 1; (1 - x/R^*)^2 \right]$, $F[\alpha, \beta, \gamma; z]$ denotes the hypergeometric series with parameters $\alpha, \beta, \gamma, x = r/\sigma$, r is the separation of the particle from the nearest point on the wall, $R^* = R/\sigma$. The wall-ionomer interaction is hydrophobic for the backbone and sidechain segments with a potential well of depth $\epsilon_{wall} = 0.33$ k_BT at the room temperature $T = 293$ K at a separation distance $r = \sigma x_{min}$. The distance x_{min} depends on the pore size R and is defined from $dU_w(x, R^*)/dx = 0$. The wall-terminal group, wall-ion, and wall-water molecule interactions are hydrophilic, which is achieved by zeroing $U_w(x, R^*)$ in Eq. (1) for distances $r > \sigma x_{min}$. The dielectric constant of the wall material and the region outside the pore is assumed to be the same as inside the pore. This simplification allows us to avoid the need to invoke the image charge concept for the dielectric discontinuity boundaries.

For the dielectric constant of the pore interior, we use a distance-dependent effective permittivity function $\epsilon(r) = 1 + (\epsilon_B - 1)(1 - r/\sigma)^{10}/(1 + (r/\sigma)^{10})$ similar to Ref. 26. This function gradually increases from $\epsilon = 1$ at small monomer-monomer separations to the bulk ionomer value $\epsilon_B = 4$. Although the best approximation for $\epsilon(r)$ can be a matter for debate,^{30,49} it is clear that the permittivity must increase with distance.

III. SIMULATION DETAILS

Simulations of hydrated ionomers inside a nanopore were performed in several stages in a process similar to that described in our previous work.²⁵⁻²⁸ Here, we shortly describe the most essential points of the procedure. We first grow, using Monte-Carlo techniques, a rigid ionomer with fixed bond length, bending and dihedral angles inside a pore of length L and radius R . For this purpose, we generate a random position inside the pore, and from that position we grow a backbone segment of length L_b . Then, regarding the middle monomer of the backbone as an attachment point for the sidechain, we grow a sidechain of length L_s from that position. Next, we generate another random point in the pore and repeat the backbone and sidechain growth procedures until all N_s backbone and N_s sidechains are grown in the pore. If a non-resolvable situation of monomer-monomer or monomer-wall overlapping occurs, a new position is sought for the backbone segment growth. At the final stage of ionomer growth, there will be $N_s(L_s + L_b)$ monomers in the pore including N_s sulfonate groups. The ionomer density ρ_{SO_3} , defined as $\rho_{SO_3} = 10^3 N_s / (V_p N_{av})$, where $V_p = \pi L R^2$ is the pore volume in cm³ and $N_{av} = 6.022 \cdot 10^{23}$ mol⁻¹ is the Avogadro constant, is given in mol/l units in Table I. For having an infinite ionomer molecule in the pore, we additionally connect backbone

TABLE I. Setup parameters for the simulation runs for the ionomers confined into a cylindrical pore of length $L = 19$ nm for the ionomers **A** and **B**, and $L = 18$ nm for the ionomer **C**. The other parameters are L_b , the number of backbone monomers between adjacent sidechains; L_s , the number of sidechain monomers; ρ_{SO_3} , the sulfonate concentration; N_S , the number of sulfonates in the cylindrical pore; R , the pore radius; γ_S , the linear density of sulfonates along the pore axis.

Ionomer	L_b	L_s	ρ_{SO_3} (mol/l)	N_S	R (nm)	γ_S (1/nm)	Run
A	14	8	1.8	1136	3.8	60	1A
				616	2.8	32	2A
				284	1.9	20	3A
				177	1.5	9	4A
				95	1.1	5	5A
				38	0.7	2	6A
B	8	8	2.3	1537	3.96	81	1B
				833	2.92	44	2B
				384	1.98	20	3B
				239	1.56	13	4B
				128	1.14	7	5B
				51	0.72	2.6	6B
C	4	8	2.8	475	2.04	26	1C
				296	1.62	16	2C
				160	1.18	9	3C
				64	0.74	3.6	4C

tips to each other by generating attractive forces between the nearest tips of different segments. Second, using again Monte-Carlo techniques, we introduce into the simulated system N_S hydronium ions and λN_S water molecules. Third, the ionomer is equilibrated against the monomer-monomer and monomer-wall potentials using 100 picosecond (ps) MD runs at constant volume and temperature. Then, in order to enhance the polymer relaxation, we temporarily detach the sidechains from the backbone and fragment the backbone into segments between the sidechain attachment points. During the next 100 ps long MD run, the fragmented system rapidly equilibrates into a new state. In the next stage, we reassemble the ionomer back to a long single molecule, equilibrate it again for another 100 ps, and pole it with an external field $E = 3$ GV/m along the pore main axis.^{25,28} Once the morphology of the ionomer is fully established over a few nanoseconds, we remove the field and perform additional equilibration of the ionomer structure for the next 100 ps. Then, during the final stage of the simulations, which typically run between 3 ns and 10 ns, we gather the necessary statistics on the quantities of interest.

In all MD runs, we use a Langevin thermostat with a friction coefficient $\gamma = 2$ ps⁻¹ and a Gaussian white-noise force of strength $6k_B T \gamma$. The equations of motion are integrated using the velocity Verlet algorithm with a time step of 0.25 fs. We impose partial periodic boundary conditions in the x -axis direction, which corresponds to the consideration of an infinite cylinder. The long-range electrostatic interactions between charged particles are handled using a one-dimensional Lekner-like summation.⁵⁰⁻⁵³

We investigate the morphology of the three different ionomer structures corresponding to a backbone segment length (the number of backbone units between adjacent

sidechains) $L_b = 4, 8$, and 14 . For all ionomer architectures, we consider the same length for sidechains, $L_s = 8$ monomers. The ionomers are placed in cylindrical pores having a radius ranging between 0.7 nm and 3.96 nm. The parameters of the simulation runs are noted in Table I. The ionomers corresponding to the runs **A** and **B** are equivalent to the bulk ionomers **A** and **B** considered in our previous work.²⁶ Also, the ionomer corresponding to run **A** coincides with the poled bulk ionomer **B** from our previous work.²⁸ In the current study, we additionally consider an ionomer with a much higher sulfonate concentration, namely the ionomer **C**. This ionomer cannot be used as a membrane in practical applications because of its mechanical instability, insufficient sulfonate clustering, and strong swelling when hydrated. However, in this study, where the stability of the ionomer is artificially fortified by the supporting walls of the pore, an increase in the sulfonate concentration inside a narrow pore might be expected to increase ionic diffusion through the cylindrical channel.³¹ For this reason, for ionomer **C**, we consider only narrow pores having a radius not exceeding 2 nm.

The ionomer **A** is closest in structure to the Nafion molecule. For each of the ionomers **A-C**, the decrease in pore radius was accomplished under conditions of constant sulfonate density, ρ_{SO_3} . In this regard, the linear density of the sulfonates, defined as $\gamma_S = N_S/L = \rho_{\text{SO}_3} \pi R^2$, is a function of the pore radius R . This parameter, as will be shown below, controls the shape of sulfonate clustering in one-dimensional geometries.

A typical snapshot from the simulation box is shown in Fig. 3, where the red lines represent the backbone segments, blue lines are for the sidechains, and the spheres represent sulfonate groups. The solvent molecules and ions are not shown. As can be seen from the snapshot picture, a well developed sulfonate clustering exists along the pore axis.

IV. RESULTS AND DISCUSSION

A. 3D ionic distribution in the pores

We start with the analyses of spatial distributions of the ions inside the pores. The three dimensional (3D) ion distributions are shown in Figs. 4-6 for the ionomers **A-C**, respectively. As an aid in understanding the ionomer morphology, the side views of the 3D distributions in the pores are supplemented by views from above (the yz projection of the simulation cell). A slight difference in the corresponding pore radii for the ionomers **A-C** is related to the hydration of sulfonates at a fixed λ . Each pore of radius R hosts a different number of sulfonates N_S for the dry ionomers **A-C**. The number N_S is defined from the condition of constant density of the ionomers for the systems **A-C**. Therefore, at a fixed hydration level $\lambda = 3$, there will be a different number of water molecules in a pore of radius R for the ionomers **A-C**. An accommodation of the different amount of water at a fixed dry ionomer density results in a slight change of the pore radius from R to $R + \delta R$. It is evident that the backbone length L_b defines the morphology of the ionomer in the pores. For example, for the ionomer **A** placed in a pore of radius 3.8 nm (run 1A), or in a pore of radius 2.8 nm (run 2A), the terminal groups develop wire-like clusters

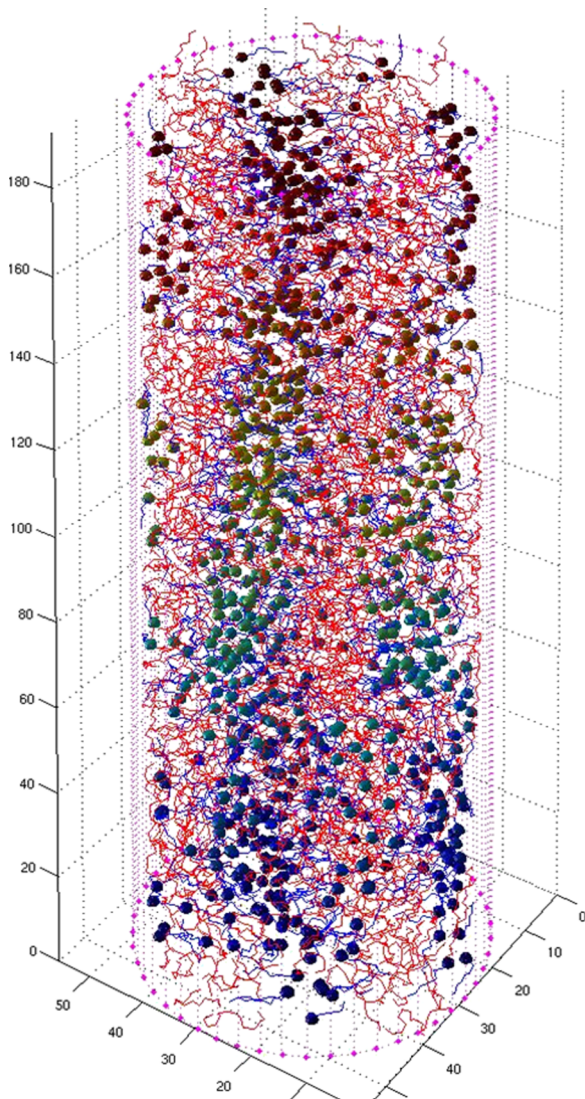


FIG. 3. Typical snapshot of simulated ionomer in a nanopore. Colored small spheres represent the sulfur atoms of the sidechain end groups. Different colors are used for different altitudes of the spheres. Ions and water molecules are not shown. Red lines denote the hydrophobic backbone segments, and blue lines the hydrophobic sidechain segments. The pore boundaries are drawn in magenta. Other parameters are the water content parameter $\lambda = 3$, backbone segment length $L_b = 14$ (ionomer **A**).

randomly occupying the pore volume along the x -axis, while the clustering of sulfonates in the ionomer **B** mostly occurs near the cylindrical walls, as seen in the corresponding results in Fig. 5 for the pores of radius 3.96 nm (run 1B) and of radius 2.92 nm (run 2B). For the run 1B, the sulfonates even form a cluster at the pore center.

In the case of larger pores, the ionic clustering in all three ionomer types has the shape of a branched wire-like network oriented parallel to the pore axis. These branched clusters transform into smooth ionic clustering in the central part of the narrow pores. This happens mostly due to strong ionomer backbone condensation at the pore walls, which makes the interior part of the channel available to the mobile ions, water molecules, and the terminal groups. Another interesting observation from Figs. 4–6 is the increased smoothness of the ionic distribution inside the smallest pores that occurs as the sulfonate density ρ_{SO_3} increases from ionomer **A** to ionomer

C. Defining the parameter $1/L_b$ as the flexibility coefficient for the ionomer backbone, we find it natural to expect that the combination $\ell_S = \gamma_S/L_b$ can be used as a meaningful measure for the sulfonate clustering in the pore. For the runs **3A–4A**, **5B**, and **4C**, where the formation of discontinued pathways of ionic distribution in narrow pores is observed, this threshold parameter is $\ell_S^c \approx 0.88$. Above this value, i.e., when $\ell > \ell_S^c$, the sulfonates form a continuous clustering in the pore, which seemingly provides a continuous channel for ion diffusion. In the opposite case, when $\ell < \ell_S^c$, the ionic clusters split into a set of compact clusters. These individual clusters show a positional ordering inside the narrow channels along the x -axis, as seen in the simulation results for runs 5A and 6A in Fig. 4, and also in the results of runs 5B and 6B in Fig. 5.

B. Details of ion, water, and sulfonate distribution in the pores

The axial modulation of ionic clusters is clearly visible from Fig. 7, where the rescaled ion densities $\rho(x)/\gamma_S$ along the pore axis are plotted. As the pore size becomes smaller, the amplitude of the density modulations in $\rho(x)$ increases in both ionomers **A** and **B**. Rough estimates show that the average cluster size is about 1.2–1.5 nm, and each cluster hosts about 9 ions in the case of pore radius 1.1 nm in ionomer **A**, and about 13 ions in the same pore radius in ionomer **B**. The clusters are highly mobile, and if their positions along the x -axis are averaged over the 100 ps long simulation time, the modulation peaks smear to a flat line.

For more detailed information about the clustering properties of terminal groups in the pores, we plot in Fig. 8 the pair correlation functions $g_{SS}(r)$ and $g_{ww}(r)$ for the sulfonates and water molecules. These functions are defined as²⁴

$$g_{ii}(r) = \frac{V}{N_i} \frac{dn_i(r)}{4\pi r^2 dr}, \quad (3)$$

where i takes values either S or w , and $dn_i(r)$ is the number of i particles located at the distance r from a fixed i atom in a shell of thickness dr . The function $g_{ii}(r)$ indicates the probability of finding two monomers i at a separation distance r averaged over the equilibrium trajectory of the simulated system. It is seen that, as the pore radius decreases from $R = 3.8$ nm to $R = 0.7$ nm according to runs 1A–6A, and correspondingly the linear density of sulfonates γ_S decreases from 76 nm^{-1} to 1.5 nm^{-1} , the height of the first maximum of $g_{SS}(r)$ decreases. This means that the correlation effects between a chosen sulfonate and an immediate neighbor from its first coordination shell become less strong. This is expected behavior, because, as the pore becomes thinner, the adsorption of the hydrophobic parts of the ionomer on the pore surface increases, making the sidechains less flexible. As a result, the sulfonates have less freedom to form clusters. This also results in a slight shift in the position of the first maximum from $r = 0.45$ nm to $r = 0.49$ nm, corresponding to runs 1A and 6A. The higher peak of the second maximum in g_{SS} at $r_{max} = 0.78$ nm for run 6A signals the formation of separated clusters along the cylindrical long axis, which is apparent upon inspecting Fig. 4. In contrast to the clustering of sulfonates, the clustering of

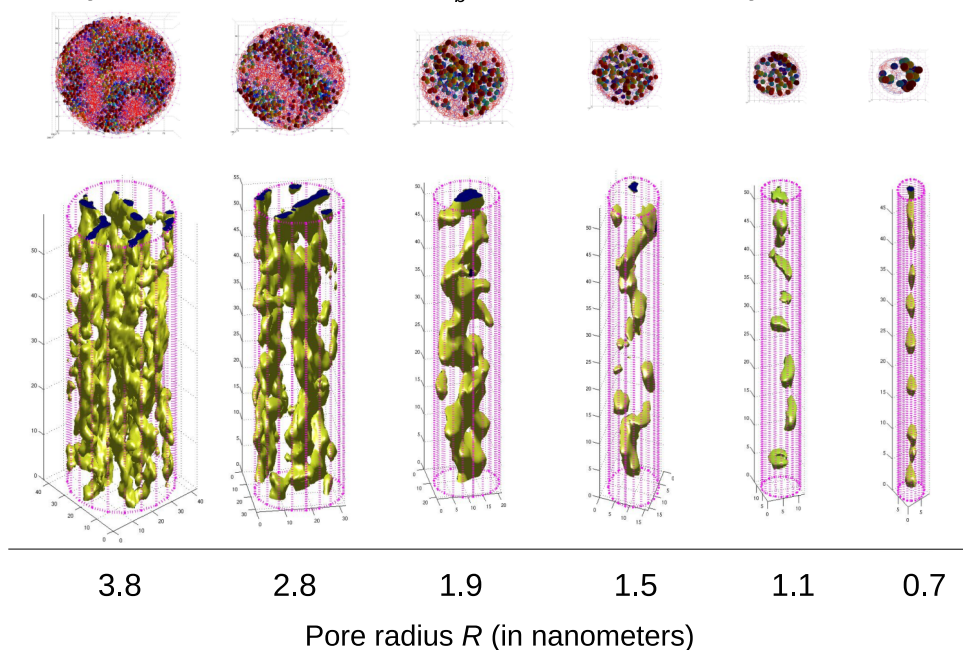
Hydrated ionomer with $L_b=14$ monomers, system **A**

FIG. 4. Simulated morphologies of ionomers with $L_b = 14$ in different pores. From left to right, the pore radius is decreased from 3.8 nm to 0.7 nm. Upper row: top view of simulation box showing the radial distribution of sulfonates. Lower row: 3D density of ions averaged over a 1 ps simulation time.

water molecules has no strong dependence on the pore radius. As seen from Fig. 8(b), the position and the height of the first maximum of $g_{ww}(r)$ stay the same for all pore sizes considered. This is mostly due to the hydrophilicity of water, the molecules of which avoid the vicinity of pore walls by forming compact clusters in the central area of the pore.

We also detect the formation of positional correlations between the ion and sulfonate radial distributions, which are

defined as

$$\rho(r) = \frac{n(r)}{2\pi r dr}, \quad (4)$$

with $n(r)$ the number of sulfonates or ions inside a cylindrical shell of thickness dr . As seen from Fig. 9, where we plot the rescaled radial densities $\rho(r)\pi R^2/N_S$ for the ions and sulfonates, there is strong radial modulation of both species.

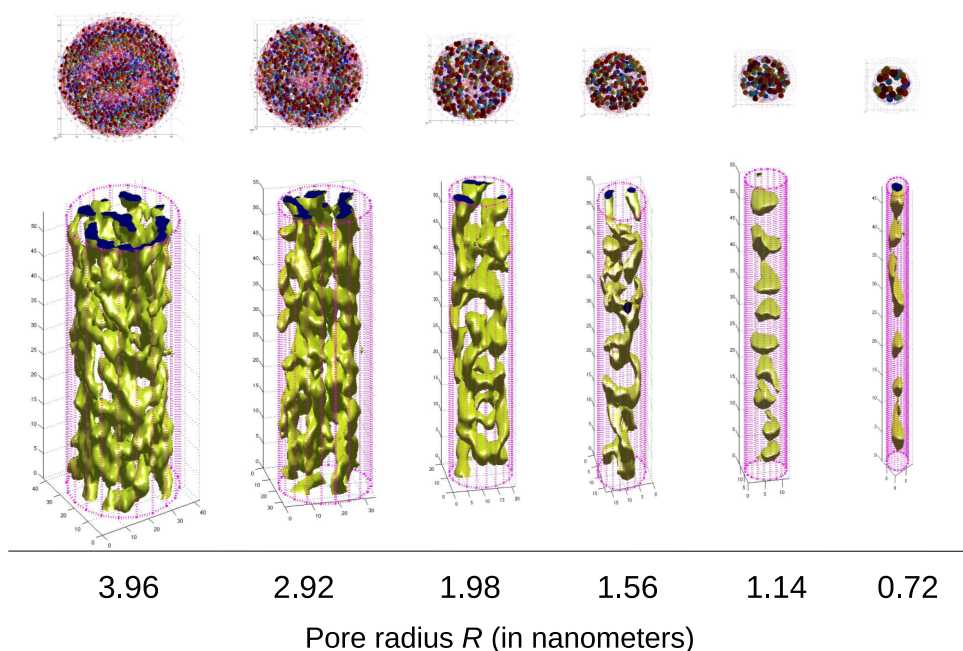
Hydrated ionomer with $L_b=8$ monomers, system **B**

FIG. 5. Simulated morphologies of ionomers with $L_b = 8$ in different pores. From left to right the pore radius is decreased from 3.96 nm to 0.72 nm. Upper row: top view of simulation box showing the radial distribution of sulfonates. Lower row: 3D density of ions averaged over a 1 ps simulation time.

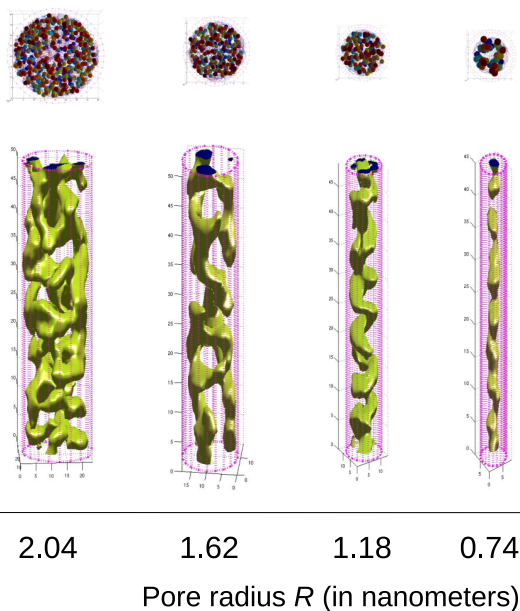
Hydrated ionomer with $L_b=4$ monomers, system **C**

FIG. 6. Simulated morphologies of ionomers with $L_b = 4$ in different pores. From left to right, the pore radius is decreased from 2.04 nm to 0.74 nm. Upper row: top view of simulation box showing the radial distribution of sulfonates. Lower row: 3D density of ions averaged over a 1 ps simulation time.

The results of the run 5B shown in Fig. 9(a) indicate the emergence of a double layer structure for both species with a phase shift of π between them. The concentration of ions is larger than the concentration of sulfonates both in the pore

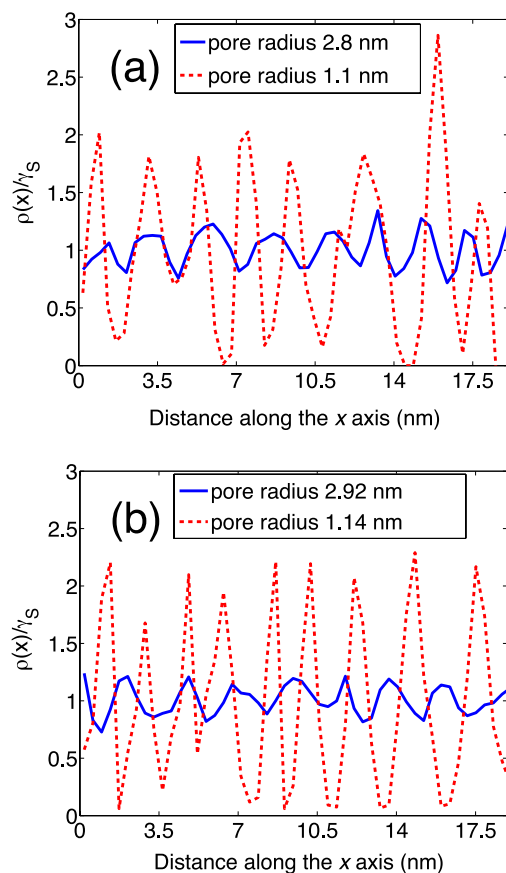


FIG. 7. Rescaled density of ions $\rho(x)/\gamma_S$ along the pore axis for the ionomers **A** and **B**. Case (a): ionomer **A**, pore radius 1.1 nm (dashed red line) and 2.8 nm (full blue line). Case (b): ionomer **B**, pore radius 1.14 nm (dashed red line) and 2.92 nm (full blue line). The appearance of the ion density modulation along the pore axis is a direct indication of ion clustering.

center and at the pore walls. The same tendency is also seen for the run 6B, shown in Fig. 9(b), but with the difference that here only a single layer of ions occupies the pore center, and the sulfonates show a maximal concentration at the half-radius of the pore.

In Fig. 10, we plot the radial distribution of ions for the runs 1A and 4A. As has been already indicated, inside the large pores, the ions tend to occupy the central part of the pore,

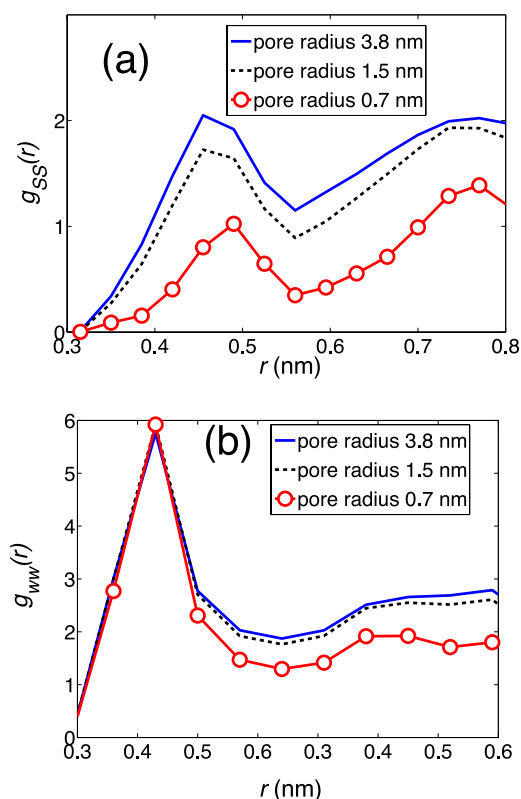


FIG. 8. Pair distributions of the terminal group sulfonates $g_{SS}(r)$ (a) and water molecules $g_{WW}(r)$ (b) are shown as a function of the separation r for the ionomer **A** and for pore radii 3.8, 1.5, and 0.7 nm.

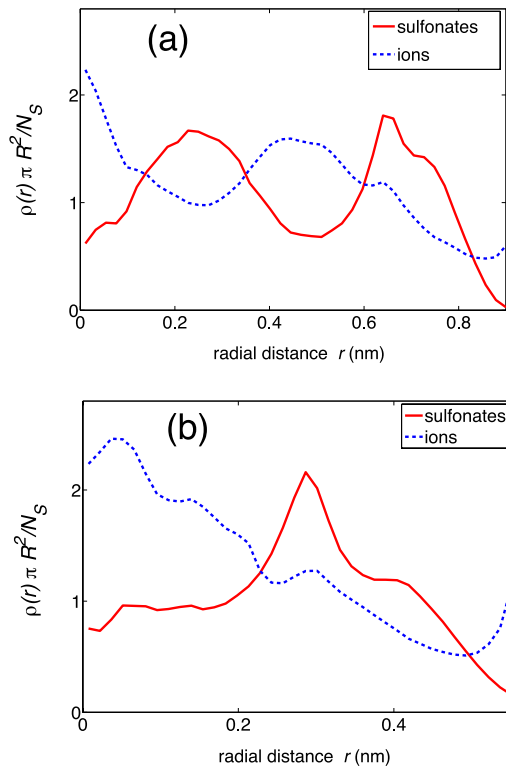


FIG. 9. Rescaled radial distributions $\rho(r)\pi R^2/N_S$ of ions and sulfonates for the narrow pores of ionomer **B** for run 5B (a) and run 6B (b). Note the emergence of a ring-like modulation of the ion and sulfonate densities with a phase shift π between them.

if that place is not already taken by sulfonate, and also stay near the pore walls because of the terminal groups in that area. This results in a radially modulated ion clustering across the pore diameter, as seen in the red solid line in Fig. 10. This radial modulation is lost in very narrow pores, where the central part of the pore becomes free of sulfonates, all of which are now condensing on the pore walls and thus available for the ions.

C. Diffusion of ions in narrow pores

In porous media, the time-dependent ion diffusion coefficient along the pore axis can be calculated from the mean

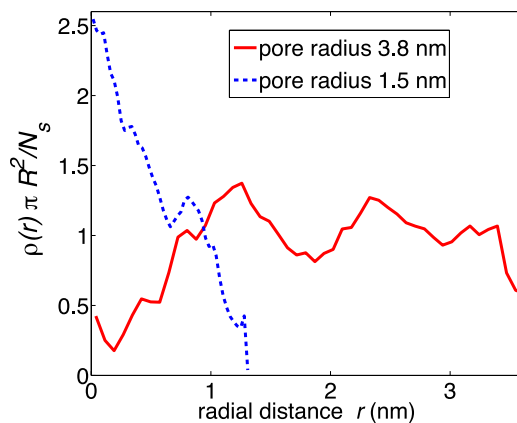


FIG. 10. Rescaled radial distributions $\rho(r)\pi R^2/N_S$ of ions in pores of radius 3.8 nm and 1.5 nm for ionomer **A** corresponding to the runs 1A and 4A. In the narrow pore the ions accumulate in the pore center, whereas in the larger pore they form ring-like modulated structures.

squared displacement of ions as

$$D_x(t) = \frac{1}{2} \frac{\langle |x(t) - x(0)|^2 \rangle}{t} \quad (5)$$

and the long-time diffusion coefficient is given by $D_x = \lim_{t \rightarrow \infty} D_x(t)$. The time evolution of the diffusion coefficients $D_x(t)$ for all three ionomers **A–C** is shown in Fig. 11. For the pore of radius 1.5 nm shown in Fig. 11(a), the ionic diffusion quickly stabilizes during the relaxation time of about $t_s \approx 0.2$ ns. However, as seen from Fig. 11(b), a much larger relaxation time of about $t_s \approx 4$ ns appears in the narrow pore of radius 0.7 nm. Below the relaxation time, the diffusion of ions gradually increases until reaching its saturation value D_{x0} . This behavior is an indication of the non-Fickian diffusion of the ions. The nearly linear increase of the diffusion coefficient as a function of the simulation time, $D_x = kt$ for $t \leq t_s$, points to the *ballistic-type* movement of ions during their relaxation. Such ballistic diffusion has been reported for single-file systems when the free movement of each file (a compact cluster or a single particle) exists before it collides with neighboring particles.^{54–58} In our system, the ballistic movement of the clusters corresponds to the movement of the ionic cluster along the pore axis until it turns into a normal Fickian diffusion at $t > t_s$. If we assume that only one cluster moves whereas all other clusters stay motionless, then the collision time between the clusters can be estimated from $t_c = \Delta x \sqrt{t_s} / \sqrt{2D_{x0}}$. Then, using the results

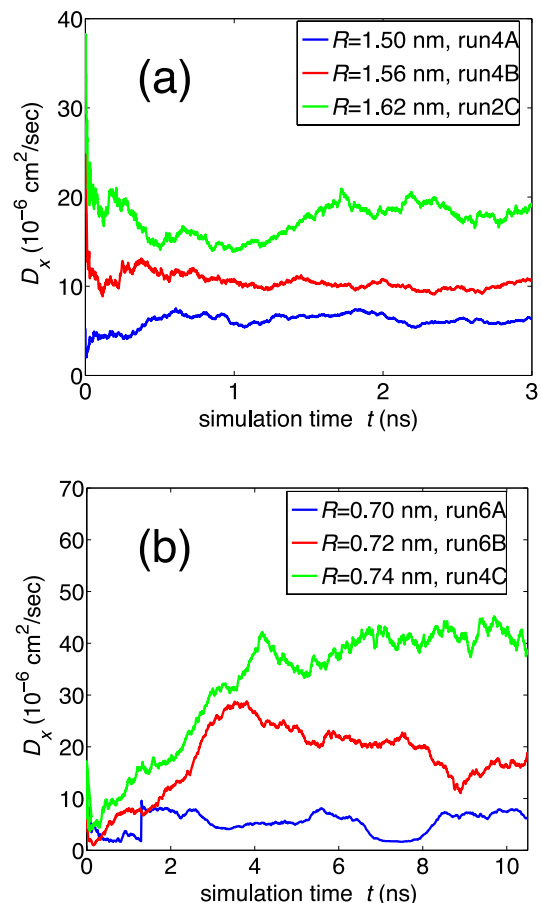


FIG. 11. Evolution of the diffusion coefficient during simulation runs lasting several nanoseconds. (a) Pore radius $R = 1.5$ nm, (b) pore radius $R = 0.7$ nm.

of run 6B for $t_s \approx 4$ ns, $D_{x0} = 20 \times 10^{-6}$ cm²/s, and the distance between clusters $\Delta x = 1$ nm, for the collision time we get $t_c \approx 1$ ns. The discrepancy by a factor of four between $t_c \approx 1$ ns and $t_s \approx 4$ ns, though acceptable for rough estimate purposes, can be understood in the following way. During the time t_c each cluster moves about 1 nm in the same direction because of the strong Coulomb repulsion along the pore axis. Therefore no collision, either actual or Coulomb, happens at $t = t_c$. At $t > t_c$ other effects, such as the change of the cluster movement direction because of the increased hindrance of the water molecules and sulfonates, interrupt the ballistic-type movement.

The dependence of the diffusion coefficient D_x on the pore size is given in Fig. 12. As the pore radius decreases, the diffusion of ions in the ionomers **A** and **B** also decreases. This initial drop is associated with the decreasing sulfonate mobility in narrow pores, where they no longer facilitate the passage of an ion from one sulfonate to the next one.⁵⁹ Nevertheless, a further decrease in the pore radius results in an increase in the ionic diffusion, as a result of the collective motion effect of ionic clusters along the pore axis. This effect is very strong for the ionomer **C**, where the ionic diffusion reaches $D_x = 40 \times 10^{-6}$ cm²/s in the pore of radius 0.7 nm. We note that this diffusion value is smaller than the proton diffusion in bulk water $D_{Bulk} \approx 70\text{--}100 \times 10^{-6}$ cm²/s at room temperature, and larger than the experimentally measured proton diffusion in Nafion, $D_{exp} \approx 4\text{--}7 \times 10^{-6}$ cm²/s. The question as to why the ionic diffusion sharply increases in narrow pores has previously been explained by the influence of the hydrophobic walls, which force the solvent to form directed hydrogen bonds parallel to the pore walls.^{20,60,61} Each water molecule in this case has only the two bonds with the water before it and the water behind it, which greatly increases its mobility. This effect indirectly also increases the mobility of solvated ions.

According to Fig. 7, the average size of a single cluster is about 1 nm, and the clusters are separated by the surface-to-surface distance of about 1 nm. Therefore, each cluster consists of about $2\gamma_s$ ions. For pore radii $0.7 \text{ nm} < R < 1.5$ nm, where the upturn of diffusion takes place, each cluster roughly has 4 to 20 ions. These ions, according to Fig. 9, mostly occupy the central part of the narrow pore. Their charge is

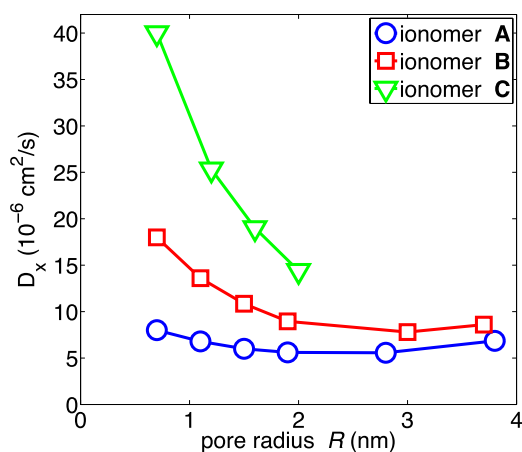


FIG. 12. Ionic diffusion coefficients D_x along the pore axis for the ionomers **A**–**C**. The pore diameters are taken from the runs in Table I.

balanced by the sulfonate head groups which show maximum concentration at about 0.3 nm off the pore axis. The electroneutrality during the ballistic movement of ions is always maintained such that the total charge of all monomers and ions inside any cylindrical slab of volume $\pi R^2 \delta L$ is zero. Our results show that the axial distribution of sulfonates follows exactly the axial distribution of protons shown in Fig. 7. We assume that the passage of the cluster through the pore channel is assisted by the back and forth movement of the sidechain tips (sulfonates), which guarantees a full electroneutrality condition in the radial direction at any given time. The expulsion of sulfonates from the pore center results in a weak screening of the ion-ion Coulomb interaction and thus increases the correlated movement of ions as a single file.

Another interesting observation is the increase of ion diffusivity when the sulfonate density increases from the ionomer **A** to the ionomer **C**. This happens because of the fact that the increased number of ions in the central pore area boosts their cooperative and directed movement due to the enhancement of long-range Coulomb correlation effects along the pore axis.

A comment should be made about the applicability of the TIP3P water model in narrow pores of runs 6A, 6B, and 4C, which do not contain enough water for bulk-like water properties. For example, visual inspection of Fig. 4 for run 6A reveals that roughly half of the tube axis area is empty of ions. Considering the strong affinity of water to ions and sulfonates, that ion-free area is also free of water molecules. Thus, the linear density of water in each cluster for run 6A is about $2\lambda\gamma_s = 12 \text{ nm}^{-1}$. This roughly makes about 4 chains of water molecules in each cluster of size 1 nm, with each chain being parallel to the pore axis and having 3 water molecules. The proton diffusion in such strongly oriented water structures is mostly defined by the Grotthuss hopping, which is a structural diffusion of protons through the network of hydrogen bonds. Such structural diffusion should be modeled using empirical valence bond (EVB) based water models.^{7,44,62} In our manuscript only the *en masse* ion diffusion is calculated using the ion mean squared displacement curves. We believe that the inclusion of the EVB mechanism into our simulation model would increase the total diffusion rate of ions.

V. CONCLUSION

We used coarse-grained simulations in a united-atom model to investigate the effect of cylindrical confinement on the morphology of Nafion-like ionomers. We showed that in narrow pores several density modulations of ions take place. First, the ions form clusters along the pore axis. Second, the ions form radially layered structures across the pore diameter. In these structures, the areas with less ionic occupancy are filled by sulfonates. Our results indicate that the hydrophobicity of the pore stabilizes the ionomer morphology by forming a continuous hydrophilic channel in the pore center. As revealed by the calculated diffusion coefficients, the one-dimensional confinement strongly enhances the mobility of ions, in contrast with what is expected in purely geometric confinement. We also detected the occurrence of significant ballistic motion of ionic clusters in narrow pores at

intermediate times. Our simulation study helps to unravel the underlying molecular principles of morphology changes and ion transport in confined ionomers.

ACKNOWLEDGMENTS

E. Allahyarov is thankful for support of this work by Russian Science Foundation (RNF) through Project No. 14-50-00124. H.L. thanks the Deutsche Forschungsgemeinschaft for support of the work through the SPP 1681 on magnetic hybrid materials. P.T. acknowledges support by the American Chemical Society Petroleum research Fund under Grant No. PRF 51995-ND7.

- ¹G. Gebel and R. B. Moore, *Macromolecules* **33**, 4850 (2000).
- ²K. A. Mauritz and R. B. Moore, *Chem. Rev.* **104**, 4535 (2004).
- ³K. D. Kreuer, S. J. Paddison, E. Spohr, and M. Schuster, *Chem. Rev.* **104**, 4637–4678 (2004).
- ⁴*Proton Exchange Membrane Fuel Cells: Materials Properties and Performance*, edited by D. P. Wilkinson, J. Zhang, R. Hui, J. Fergus, and X. Li (CRC Press and Science, 2009).
- ⁵*Issues in Hydrogen, Fuel Cell, Electrochemical, and Experimental Technologies*, 2013 ed., edited by Q. Ashton Acton (ScholarlyEditions and Technology & Engineering, 2013).
- ⁶*Device and Materials Modeling in PEM Fuel Cells*, edited by S. J. Paddison and K. S. Promislow (Springer Science, 2009).
- ⁷S. Walbran and A. A. Kornyshev, *J. Chem. Phys.* **114**, 10039 (2001).
- ⁸A. A. Kornyshev, A. M. Kuznetsov, E. Spohr, and J. Ulstrup, *J. Phys. Chem. B* **107**, 3351 (2003).
- ⁹P. Choi, N. H. Jalani, and R. Datta, *J. Electrochem. Soc.* **152**, E123 (2005).
- ¹⁰Y. S. Kim, F. Wang, M. Hickner, S. McCartney, Y. T. Hong, W. Harrison, Th. A. Zawodzinski, and J. E. McGrath, *J. Polym. Sci., Part B: Polym. Phys.* **41**, 2816 (2003).
- ¹¹M. Saito, K. Hayamizu, and T. Okada, *Phys. Chem. B* **109**, 3112 (2005).
- ¹²K. D. Kreuer, *J. Membr. Sci.* **185**, 29 (2001).
- ¹³K. M. Lee, R. Wycisk, M. Litt, and P. N. Pintauro, *J. Membrane Sci.* **383**, 254 (2011).
- ¹⁴M. Litt, S. Granados-Focil, and J. Kang, *Fuel Cell Chem. Oper.* **1040**, 49 (2010).
- ¹⁵H. Xiang, K. Shin, T. Kim, S. I. Moon, T. J. McCarthy, and T. P. Russell, *Macromolecules* **37**, 5660–5664 (2004).
- ¹⁶R. M. Penner and C. R. Martin, *J. Electrochem. Soc.* **132**, 514 (1985).
- ¹⁷M. P. Rodgers, J. Berrington, S. Holdcroft, and Z. Shi, *J. Membr. Sci.* **321**, 100 (2008).
- ¹⁸F. M. Vichi, M. T. Colomer, and M. A. Anderson, *Electrochem. Solid-State Lett.* **2**, 313 (1999).
- ¹⁹K. Schmidt-Rohr and Q. Chen, *Nat. Mater.* **7**, 75 (2008).
- ²⁰S. Joseph and N. R. Aluru, *Nano Lett.* **8**, 452 (2008).
- ²¹E. Allahyarov and P. L. Taylor, *J. Chem. Phys.* **127**, 154901 (2007).
- ²²E. Allahyarov and P. L. Taylor, *Phys. Rev. E* **80**, 020801(R) (2009).
- ²³E. Allahyarov and P. L. Taylor, *J. Phys. Chem. B* **113**, 610 (2009).
- ²⁴E. Allahyarov, P. L. Taylor, and H. Löwen, *Phys. Rev. E* **80**, 061802 (2009).
- ²⁵E. Allahyarov, P. L. Taylor, and H. Löwen, *Phys. Rev. E* **81**, 031805 (2010).
- ²⁶E. Allahyarov and P. L. Taylor, *J. Polym. Sci., Part B: Polym. Phys.* **49**, 368 (2011).
- ²⁷E. Allahyarov, P. L. Taylor, and H. Löwen, *J. Phys.: Condens. Matter* **23**, 234105 (2011).
- ²⁸E. Allahyarov, P. L. Taylor, and H. Löwen, *J. Phys.: Condens. Matter* **23**, 455102 (2011).
- ²⁹Y. Yang and P. N. Pintario, *Ind. Eng. Chem. Res.* **43**, 2957 (2004).
- ³⁰S. J. Paddison, *Annu. Rev. Mater. Res.* **33**, 289 (2003).
- ³¹M. Eikerling, A. A. Kornyshev, A. M. Kuznetsov, J. Ulstrup, and S. Walbran, *J. Phys. Chem. B* **105**, 3646 (2001).
- ³²M. A. Ilhan and E. Spohr, *J. Electroanal. Chem.* **660**, 347 (2011).
- ³³A. Vishnyakov and A. V. Neimark, *J. Phys. Chem. B* **105**, 7830 (2001).
- ³⁴S. Yamamoto, R. Jinnouchi, Sh. Yamakawa, and Sh. Hyodo, in *14th International Conference on the Properties of Water and Steam, Kyoto, Japan* (Maruzen Co., Ltd., 2004), p. 411.
- ³⁵P. Commer, C. Harting, D. Seeliger, and E. Spohr, *Mol. Simul.* **30**, 755 (2004).
- ³⁶K. Malek, M. Eikerling, Q. Wang, Z. Liu, Sh. Otsuka, K. Akizuki, and M. Abe, *J. Chem. Phys.* **129**, 204702 (2008).
- ³⁷S. Yamamoto, *Nippon Gomu Kyokaishi* **77**, 130 (2004).
- ³⁸K. Malek, M. Eikerling, Q. Wang, T. Navessin, and Z. Liu, *J. Phys. Chem. C* **111**, 13627 (2007).
- ³⁹J. T. Wescott, Y. Qi, L. Subramanian, and T. W. Capehart, *J. Chem. Phys.* **124**, 134702 (2006).
- ⁴⁰L. Pisani, M. Valentini, D. H. Hofmann, L. N. Kuleshova, and B. D'Aguzzo, *Solid State Ionics* **179**, 465 (2008).
- ⁴¹D. Brandell, J. Karo, A. Liivat, and J. O. Thomas, *J. Mol. Model.* **13**, 1039 (2007).
- ⁴²A. Venkatnathan, R. Devanathan, and M. Dupuis, *J. Phys. Chem. B* **111**, 7234 (2007).
- ⁴³S. J. Paddison and T. A. Zawodzinski, *Solid State Ionics* **113-115**, 333 (1998).
- ⁴⁴E. Spohr, P. Commer, and A. A. Kornyshev, *J. Phys. Chem. B* **106**, 10560 (2002).
- ⁴⁵M. W. Mahoney and W. L. Jorgensen, *J. Chem. Phys.* **112**, 8910 (2000).
- ⁴⁶E. L. Thompson, T. W. Capehart, T. J. Fuller, and J. Jorne, *J. Electrochem. Soc.* **153**, A2351 (2006).
- ⁴⁷G. J. Tjatjopoulos, D. L. Feke, and J. A. Mann, Jr., *J. Phys. Chem.* **92**, 4006 (1988).
- ⁴⁸Y. W. Tang, I. Szalai, and K. Y. Chan, *J. Phys. Chem. A* **105**, 9616 (2001).
- ⁴⁹P. L. Taylor, B. C. Xu, F. A. Oliveira, and T. P. Doerr, *Macromolecules* **25**, 1694 (1992).
- ⁵⁰J. C. G. Montoro and J. L. F. Abascal, *J. Chem. Phys.* **109**, 6200 (1998).
- ⁵¹R. Paul and S. J. Paddison, *J. Chem. Phys.* **123**, 224704 (2005).
- ⁵²M. Mazars, *J. Chem. Phys.* **115**, 2955 (2001).
- ⁵³N. Grönbeck-Jensen, G. Hummer, and K. M. Beardmore, *Mol. Phys.* **92**, 941 (1997).
- ⁵⁴A. Taloni and M. A. Lomholt, *Phys. Rev. E* **78**, 051116 (2008).
- ⁵⁵A. Taloni and F. Marchesoni, *Phys. Rev. E* **74**, 051119 (2006).
- ⁵⁶F. Marchesoni and A. Taloni, *Phys. Rev. Lett.* **97**, 106101 (2006).
- ⁵⁷C. Lutz, M. Kollmann, and C. Bechinger, *Phys. Rev. Lett.* **93**, 026001 (2004).
- ⁵⁸A. Striolo, *Nano Lett.* **6**, 633 (2006).
- ⁵⁹S. Dokmaijrijan and E. Spohr, *J. Mol. Liq.* **129**, 92 (2006).
- ⁶⁰D. J. Mann and M. D. Halls, *Phys. Rev. Lett.* **90**, 195503 (2003).
- ⁶¹C. Dellago, M. M. Naor, and G. Hummer, *Phys. Rev. Lett.* **90**, 105902 (2003).
- ⁶²U. W. Schmitt and G. A. Voth, *J. Phys. Chem. B* **102**, 5547 (1998).